Carbon Nanotube-Bridged Graphene 3D Building Blocks for Ultrafast Compact Supercapacitors

Duy Tho Pham,[†,‡] Tae Hoon Lee,[†,‡] Dinh Hoa Luong,[†,‡] Fei Yao,[†] Arunabha Ghosh,[†] Viet Thong Le,[†,‡] Tae Hyung Kim,[†] Bing Li,[†,‡] Jian Chang,[†,‡] and Young Hee Lee*[,†,‡]

[†]IBS Center for Integrated Nanostructure Physics, Institute for Basic Science, Sungkyunkwan University, Suwon 440-746, Republic of Korea and
[‡]Department of Energy Science, Department of Physics, Sungkyunkwan University, Suwon 440-746, Republic of Korea

ABSTRACT The main obstacles to achieving high electrochemical energy density while retaining high power density are the trade-offs of energy *versus* power and gravimetric *versus* volumetric density. Optimizing structural parameters is the key to circumvent these trade-offs. We report here the synthesis of carbon nanotube (CNT)-bridged graphene 3D building blocks *via* the Coulombic interaction between positively charged CNTs grafted by cationic surfactants and negatively charged graphene oxide sheets, followed by KOH activation. The CNTs were intercalated into the nanoporous graphene layers to build pillared 3D structures, which enhance accessible surface area and allow fast ion diffusion. The resulting graphene/CNT films are free-standing and flexible with a high electrical conductivity of 39 400 S m^{-1} and a reasonable mass density of 1.06 g cm^{-3}. The supercapacitors fabricated using these films exhibit an outstanding electrochemical performance in an ionic liquid electrolyte with a maximum energy density of 117.2 Wh L^{-1} or 110.6 Wh kg^{-1} at a maximum power density of 424 kW L^{-1} or 400 kW kg^{-1}, which is based on thickness or mass of total active material.

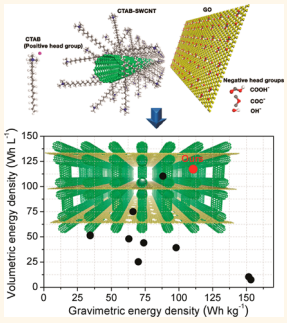

KEYWORDS: graphene · carbon nanotubes · hybrids · self-assembly · KOH activation · supercapacitors

Unlike batteries, which store energy through intercalation or chemical reactions and have low power density, supercapacitors or ultracapacitors operate *via* the electrical double-layer capacitance (EDLC) formed at an electrode−electrolyte interface or *via* pseudocapacitance involving charge transfers during surface chemical reactions, which delivers high power density with a reasonable number of cycles.[1,2] However, both the gravimetric and volumetric energy densities of current state-of-the-art supercapacitors (4−5 Wh kg^{-1} and 5−8 Wh L^{-1}) are much lower than those of lead-acid batteries (26−34 Wh kg^{-1} and 50−90 Wh L^{-1}).[3−5] Attempts over the last century to improve the energy density of rechargeable batteries have resulted in only a 6-fold increase.[6] By contrast, efforts in recent decades to simultaneously improve the energy and power density of capacitors have been extremely efficient and increased the energy density by several orders of magnitude.[7]

Graphene-based materials, with light mass, high electrical conductivity, mechanical strength, and specific surface area as well as mass production in tons of quantities at low cost,[4,8,9] are expected as promising candidates that can satisfy high-energy storage requirements for supercapacitors. A series of studies have been done to achieve high values of gravimetric energy densities using graphene-based materials, including curved graphene,[10] oriented graphene hydrogel,[11] laser-scribed graphene,[12] activated graphene,[4,13−17] and electrolyte-mediated chemically converted graphene (EM-CCG).[5] Nevertheless, they still suffer from either mediocre volumetric energy densities due to their low mass densities or medium power densities due to their low intrinsic electrical conductivity. Recently, a large family of 2D transition metal carbides labeled MXenes was employed as electrode materials for supercapacitors.[18,19] These materials exhibit high gravimetric capacitance and ultrahigh volumetric capacitance, while retaining high power density due to their very high mass densities and good intrinsic electrical conductivity. The safety issue, cost, and large-scale production of the material processing route yet need to

* Address correspondence to leeyoung@skku.edu.

Received for review December 12, 2014 and accepted February 1, 2015.

Published online February 01, 2015
10.1021/nn507079x

be investigated further to meet the requirement of practical applications.

One limit of graphene-based supercapacitors is the restacking of graphene layers *via* van der Waals interactions during reduction.[12,20] To prevent this restacking, one-dimensional CNTs were used as a smart spacer.[21−31] CNTs not only prevent graphene from restacking to increase the accessible surface area but also act as efficient electrical conducting paths to improve the power. The performance continues to be poor because of either simple mixtures of CNT/graphene where CNTs are not intercalated into graphene or intercalated CNT/graphene hybrids but without nanoscale pores in the graphene layers, which limited ion diffusion.[32] The issue is how to accommodate CNTs within the graphene to increase the accessible surface area while creating efficient ion diffusion pathways. Another issue is the optimum mass density during structural design because either high or low mass density will sacrifice gravimetric or volumetric density. The CVD-grown vertically aligned CNT/graphene hybrids give low mass density (<0.4 g cm^{-3}), which cannot overcome the trade-off between volumetric and gravimetric energy density, let alone the controllability of CNT density.[21,30,31] On the other hand, the chemically bonded graphene/CNT gives a high mass density of ~1.5 g cm^{-3}, which resulted in the low gravimetric energy density.[26]

Herein, we report the fabrication of supercapacitors based on free-standing, flexible, and highly conducting films consisting of stacked nanoporous graphene layers pillared with single-walled carbon nanotubes (SWCNTs). Due to this unique 3D porous structure of the electrodes, a remarkable electrochemical performance of the fabricated supercapacitors was achieved with a maximum energy density of 117.2 Wh L^{-1} or 110.6 Wh kg^{-1} at a maximum power density of 424 kW L^{-1} or 400 kW kg^{-1}, based on the thickness or mass of the total active material.

RESULTS AND DISCUSSION

The ac-Gr/SWCNTs films were prepared *via* the Coulombic self-assembly of graphene oxide (GO) and SWCNTs, followed by a simple KOH activation (see Experimental Section and Supporting Information Figure S1). The schematic of the sample fabrication is shown in Figure 1. Positively charged SWCNTs with a zeta potential of +55.9 mV at pH 7 (Supporting Information Figure S2a) were obtained by grafting to a cationic surfactant (cetyltrimethylammonium bromide: CTAB).[33] Negatively charged GO sheets exhibit a zeta potential of −53.4 mV at pH 7 (Supporting Information Figure S2b) in deionized (DI) water because of their functional groups such as carboxylic acid ($COOH^-$), epoxy (COC^-), and hydroxyl (OH^-).[34−36] Other structural properties of the CTAB-grafted SWCNTs

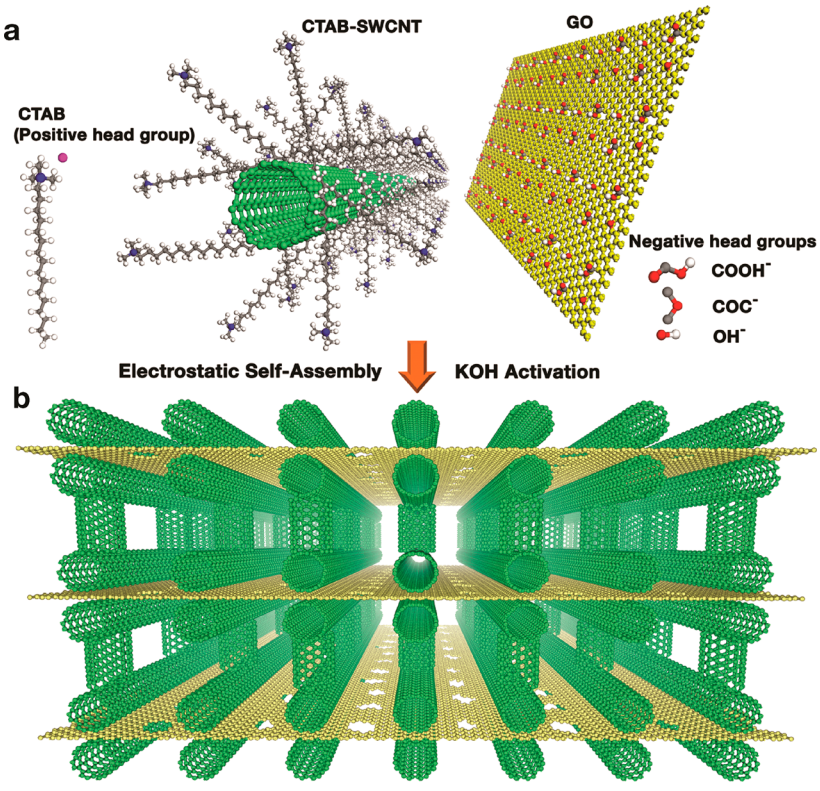

Figure 1. Schematic for fabricating the ac-Gr/SWCNT hybrid nanostructure. (a) The CTAB-grafted SWCNTs are positively charged, and the GO layers are negatively charged due to their functional groups. (b) Schematic of the 3D SWCNT-bridged graphene block. KOH activation generates nanoscale pores in the graphene layers, which are expected to provide a simple means of ion diffusion.

(CTAB-SWCNTs) and GO are shown in Supporting Information Figure S4c–e and Table S1. The GO/SWCNT mass ratio was controlled by concentrations of the GO and CTAB-SWCNT solutions. The KOH solution was added after mixing the GO and CTAB-SWCNTs. Activating or annealing at high temperature (800 °C) not only reduced the GO functional groups but also created nanoscale pores in both the SWCNTs and graphene layers.[4] This result provides a simple route for efficient ion diffusion while insignificantly sacrificing the mass density.

The free-standing and flexible ac-Gr/SWCNT film prepared using a GO/SWCNT mass ratio of 3:1 with a 6 M KOH solution is shown in Figure 2a. A top-view scanning electron microscopy (SEM) image of the film (Figure 2b) showed entangled SWCNTs and fragmented graphene flakes (dotted lines). Transmission electron microscopy (TEM) was also performed to see the nanoscale pores on graphene layers as shown in Supporting Information Figure S3. The cross-sectional SEM image revealed SWCNTs dangling from the graphene layer edge (Figure 2c). Notably, some SWCNTs seemed to be vertically aligned between the graphene layers despite the artificial enlargement of the interlayer that occurred during the SEM sample preparation (Figure 2d and cross-sectional SEM images in Supporting Information Figure S4). To visualize the SWCNT alignment, polarized Raman spectroscopy was performed by illuminating a cross-section of the sample with a laser (Supporting Information Figure S5). The G-band intensity was maximized at 0° and decreased consistently with increasing polarized angle (Figure 2e). At 90°, where the polarizer director is perpendicular to the CNT axis, the G-band intensity was minimized with a 62% reduction. Because some portion of the SWCNTs was randomly distributed on the graphene layers, their contribution may not be negligible. Therefore, we prepared another Gr/SWCNT sample using sodium dodecyl sulfate-grafted SWCNTs (SDS-SWCNTs) while holding the GO/SWCNT mass ratio at 3:1 (see Experimental Section). All of the SWCNTs were randomly distributed on the graphene

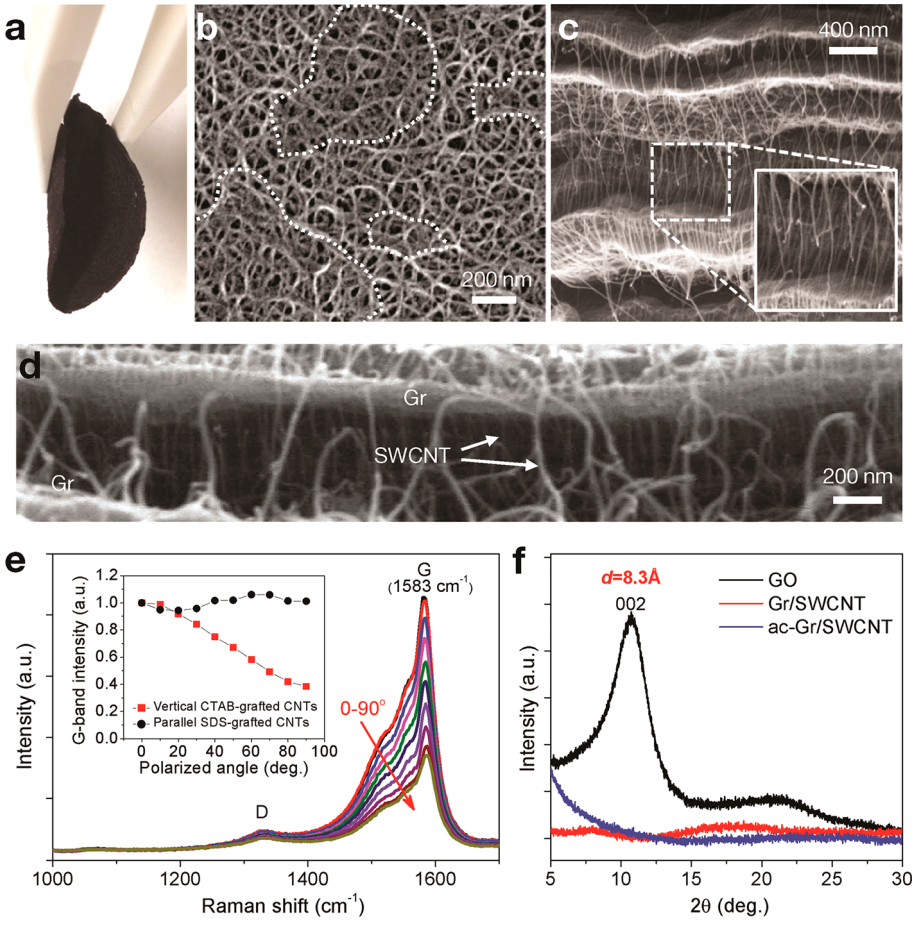

Figure 2. Structural properties of the ac-Gr/SWCNT film. (a) Optical micrograph showing the free-standing and flexible film. (b) Top-view SEM image showing the porous SWCNT network and remaining graphene flakes (dotted lines). (c) Cross-sectional SEM image containing dangling SWCNTs (magnified in the inset). (d) Magnified cross-sectional SEM image at another point that clearly shows vertical SWCNTs between the graphene layers in the inner part. (e) Polarized Raman spectra of the G-band intensity near 1583 cm^{-1}. This intensity significantly decreases as the angle between the polarizer and the long SWCNT axis approaches 90°. The inset shows the intensity variance *versus* the angle. Similar data points for the sample of parallel SDS-grafted SWCNTs to graphene. (f) XRD patterns of GO, nonactivated Gr/SWCNT, and ac-Gr/SWCNT samples.

layer without any perpendicular components because of the similarity of the negatively charged SDS-SWCNTs to the GO. Although the G-band intensity showed some oscillation due to the contribution from both graphene and the SWCNTs with a maximum that deviated from 90°, the magnitude was much smaller than that observed for the ac-SWCNT/Gr sample (the inset of Figure 2e and Supporting Information Figure S6b). These results strongly imply that a large portion of SWCNTs formed a preferentially aligned liquid-crystalline phase perpendicular to the graphene layers.

X-ray diffraction (XRD) patterns were obtained to observe the graphene and SWCNT stacking (Figure 2f). The GO film showed a broad (002) peak with an interlayer spacing of 8.3 Å. This peak disappeared after the self-assembly of GO with SWCNTs. This disappearance was due to the intercalation of the positively charged CTAB-SWCNTs into the negatively charged GO layers, which prevented the graphene from restacking and contrasts with the SDS-SWCNT/Gr sample (see Supporting Information Figure S6c). The KOH treatment did not alter this restacking behavior. Functional groups of GO were removed after high-temperature annealing in the KOH activation process, as indicated by the significantly reduced D-band intensity in the Raman spectrum (Supporting Information Figure S7). This led to the high electrical conductivity of the films. The small D-band remaining after the KOH activation was mostly due to the damaged graphene layers. Brunauer–Emmett–Teller (BET) surface area of the ac-Gr/SWCNT film increased to 652 $m^2\ g^{-1}$ from 471 $m^2\ g^{-1}$ of the nonactivated Gr/SWCNT sample (Supporting Information Figure S8 and Table S2). The micropore (0.25 mL g^{-1}) and mesopore volume (0.23 mL g^{-1}) were also well developed. Forming an appropriate distribution of micropores and mesopores further ensures rapid ion diffusion and can enhance the power density.

Another advantage of our structure is the medium mass density (1.06 g cm^{-3}) and high electrical conductivity (39 400 S m^{-1}) (Supporting Information Figure S9), which is important to obtain both high volumetric and gravimetric (energy and power) densities. It is worth noting that large gaps (~200–500 nm) as seen in cross-sectional SEM images (Figure 2c,d and Supporting Information Figure S4c,d) are maybe not the intrinsic interlayer distance. These large gaps may come from the expansion of graphene layers during sample preparation for SEM measurement and should be subtracted from the thickness (one such example is shown in Supporting Information Figure S9a). To obtain accurate thickness, the flexible ac-Gr/SWCNT films were gently broken after dipping into liquid nitrogen, and their thicknesses were measured several times by cross-sectional SEM at different places; then the average thickness (t) was calculated. The mass density (ρ) of the films was calculated by ρ = area density/t. Here, the area density was measured previously. The electrical conductivity (σ) was also calculated based on the average thickness t and the sheet resistance (R_s) of the films (see Experimental Section).

The previous report shows that chemically bonded graphene/CNT gives a mass density of ~1.5 g cm^{-3}.[26] This value is similar to that (1.48 g cm^{-3}) of our control sample, where CNTs and graphene layers were simply mixed with SDS surfactant (no pillared structures are formed in this case) (see Supporting Information Figure S6). Meanwhile, the CVD-grown vertically aligned CNT/graphene hybrids give a low mass density (<0.4 g cm^{-3}) due to sparse distribution and long length of vertically aligned CNTs.[21,30,31] In our sample, the vertically aligned CNTs are short and highly packed, which is demonstrated by the strong angle dependence of the Raman G-band intensity and a decrease of the intensity value by 62% at 90 deg (Figure 2e). Therefore, the value of 1.06 g cm^{-3} of our CNT-pillared graphene films seems to be reasonable. The high electrical conductivity may be attributed to the conjunction between graphene and SWCNTs in which they are interlinked to each other *via* just simple contact or covalent bonds.[29,31,37] Since the D-band intensity in the Raman spectroscopy did not reveal a distinct difference after the sample process (see Supporting Information Figure S7), it is unlikely that the junction is covalently bonded.

To demonstrate the electrochemical performance of the ac-Gr/SWCNT electrodes, we constructed a series of supercapacitors using a coin-cell configuration with neat 1-ethyl-3-methylimidazolium tetrafluoroborate (EMIM BF_4) as an ionic liquid electrolyte (see Experimental Section). We first optimized the GO/SWCNT mass ratio and KOH concentration for preparing the the ac-Gr/SWCNT samples (Figure 3). The GO/SWCNT mass ratio of 3:1 exhibited the highest capacitance (Figure 3a; see also Supporting Information Figure S10). Meanwhile, the capacitance was improved as the KOH concentration increased from 6 to 8 M (Figure 3b; see also Supporting Information Figure S11). This capacitance improvement is attributed to the generation of rich nanoscale pores on graphene/SWCNT layers when more KOH content was supplied for the activation process. However, the sample was severely damaged at KOH concentrations above 8 M due to violent attacks on the carbon network by a large quantity of KOH.

Electrochemical impedance spectroscopy (EIS) showed the nearly perpendicular line in the low-frequency region for the optimized ac-Gr/SWCNT sample, which demonstrates the ideal capacitive behavior of the cell with rapid ion diffusion (Figure 4a).[4,5] The tangential angle was low for the nonactivated Gr/SWCNT sample, indicating poor ion diffusion. The semicircle of the optimized ac-Gr/SWCNT sample was ~10 Ω, which is small enough compared to other reports with ionic liquids,[4,5,14,24] although this value is still larger than that with aqueous

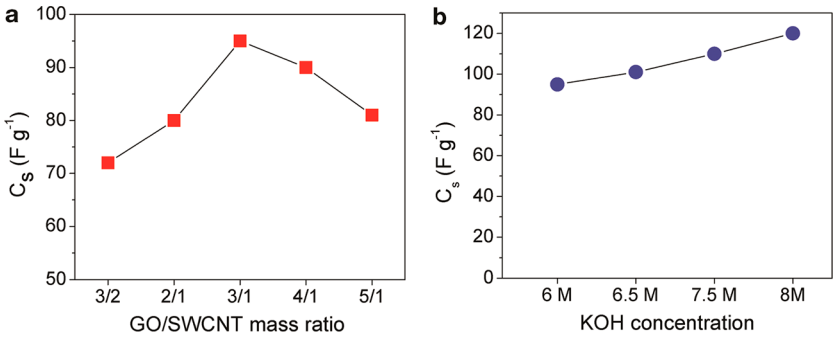

Figure 3. Optimized processing condition for the ac-Gr/SWCNT electrodes. The gravimetric specific capacitance of the ac-Gr/SWCNT electrodes obtained at a scan rate of 200 mV s^{-1} as a function of (a) GO/SWCNT mass ratio and (b) KOH concentration.

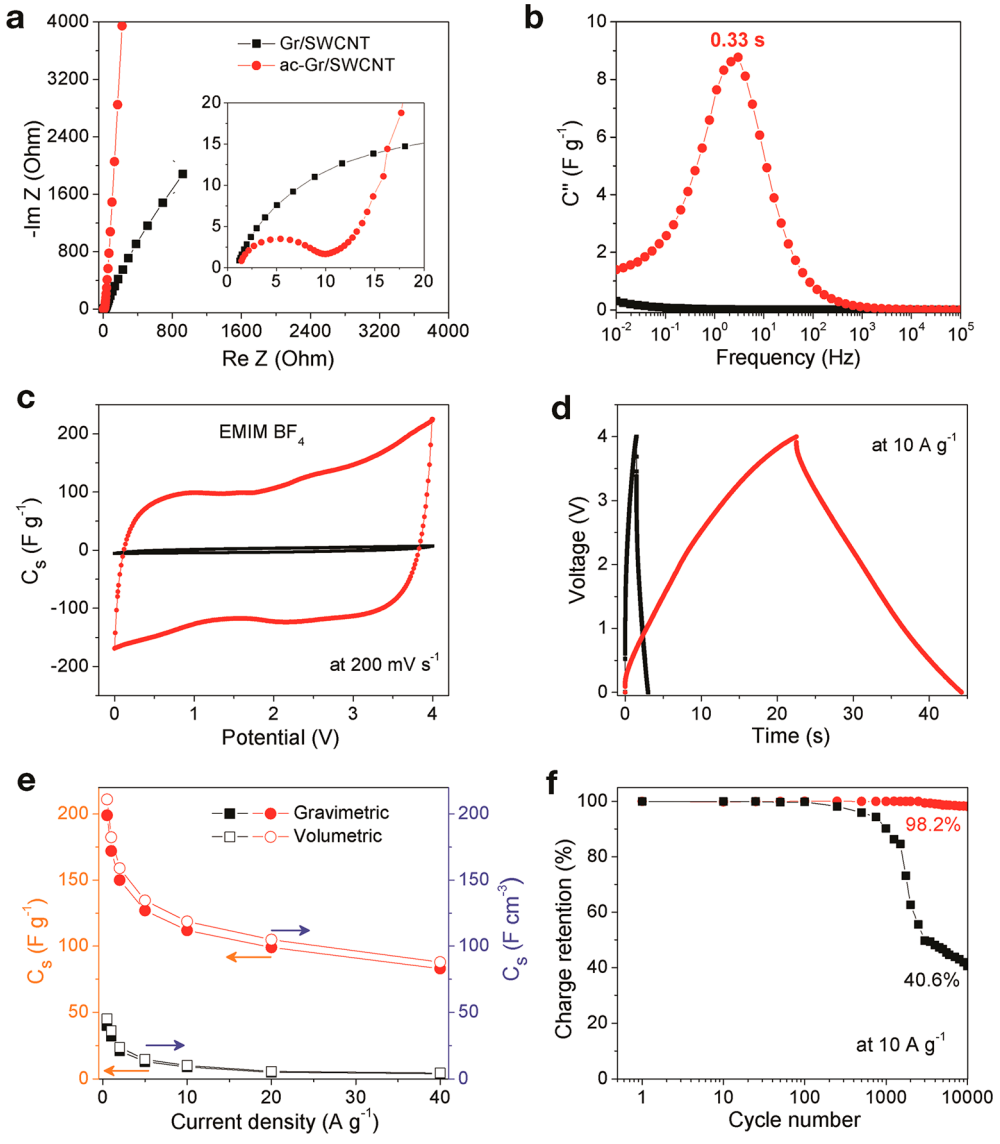

Figure 4. Electrochemical performance of the optimized ac-Gr/SWCNT electrode. The nonactivated Gr-SWCNT sample is shown as a reference. (a) Nyquist plot revealing the nearly ideal capacitive behavior of the cell. The inset shows a magnified view of the high-frequency region. (b) Plot of the imaginary capacitance *versus* the frequency showing the low relaxation time, 0.33 s, which indicates rapid ion diffusion. (c) CV curves at a scan rate of 200 mV s^{-1} with a nearly rectangular shape, indicating an efficient EDLC. (d) CD curves at a current density of 10 A g^{-1}. (e) Gravimetric and volumetric specific capacitances as a function of the current density. (f) Cyclic stability. A capacitance retention of 98.2% was observed after 10 000 cycles at a current density of 10 A g^{-1}.

electrolytes.[5,11,12] Nevertheless, an ionic liquid is certainly advantageous over an aqueous solution to achieve high energy density due to a large potential window. Plotting the imaginary capacitance *versus* the frequency (Figure 4b) yields the relaxation time, also called the RC time constant, which is a measure of the time required to discharge 50% of the total energy stored in the device.[28,38] The obtained value, 0.33 s, indicates rapid ion diffusion within the optimized ac-Gr/SWCNT electrode. This result contrasts with the Gr/SWCNT sample, which exhibited an extremely slow relaxation time.

Cyclic voltammetry (CV) curves were obtained at a scan rate of 200 mV s^{-1} (Figure 4c). The optimized ac-Gr/SWCNT sample exhibited a nearly rectangular shape with large area from 0 to 4 V, which indicates an efficient EDLC formation.[12] In contrast, the Gr/SWCNT sample exhibited negligible charge storage. Nearly triangular galvanostatic charge/discharge (CD) curves were observed at a current density of 10 A g^{-1} with a small *IR* drop of 0.0125 Ω·g (Figure 4d). More information on the electrochemical performance of the optimized ac-Gr/SWCNT sample is shown in Supporting Information Figure S12. The specific capacitance (C_s) was obtained from the discharge curves. Both the gravimetric C_s (F g^{-1}) and volumetric C_s (F cm^{-3}) values were examined using the following relationship: volumetric C_s = electrode mass density × gravimetric C_s.[5] With a reasonable density of 1.06 g cm^{-3} of the optimized ac-Gr/SWCNT film, both high values of 199 F g^{-1} and 211 F cm^{-3} were achieved at a current density of 0.5 A g^{-1}, while relatively large values (99 F g^{-1} and 105 F cm^{-3}) were retained at a high current density of 20 A g^{-1} (Figure 4e). By assuming the maximum EDLC of carbon-based materials is ~21 μF cm^{-2},[39] and all the BET surface area (652 m^2 g^{-1}) of the optimized ac-Gr/SWCNT electrode is accessible by electrolyte ions, a maximum calculated C_s is 652 m^2 g^{-1} × 21 μF cm^{-2} ≈ 137 F g^{-1}, which is smaller than 199 F g^{-1} of the measured value at low rate (0.5 A g^{-1}). This strongly suggests that another contribution of pseudocapacitance exists in addition to EDLC. The slight nonrectangular CV curves and nonlinear triangular CD curves at low rates originate from pseudocapacitive behavior, which is attributed to the oxygen-related functional groups that exist on the surface of the ac-Gr/SWCNT samples, supported by an energy dispersive X-ray spectroscopy (EDS) estimate of an oxygen content of 4.5 wt % (Figure S4b). A capacitance retention of 98.2% was observed after 10 000 cycles at a discharge current density of 10 A g^{-1} (Figure 4f), indicating the high electrochemical stability of the electrode. In contrast, the Gr/SWCNT sample exhibited very poor capacitance and capacitance retention. Moreover, the cycling test over 5000 cycles at relatively low dischange current density (1 A g^{-1}) also revealed the high capacitance retention (94.7%) (Supporting Information Figure S12d). Nyquist plots and SEM images of the optimized ac-Gr/SWCNT electrode before and after cycling are shown in Supporting Information Figure S12e and Figure S13, respectively. The EIS was insignificantly changed and the structural morphology was still retained after the cycling test. These results again confirm the high electrochemical stability of the device.

It is worth noting that the neat EMIM BF_4 ionic liquid has an electrochemical window from −2.2 to 3.5 V. In our case, the nearly rectangular CV curve was maintained from 0 to 4 V, ensuring electrolyte stability. On the other hand, at larger potential windows (4.5−6 V), the chemical reaction peaks above 4 V emerged and the current increased rapidly at high voltage, indicating electrolyte reaction or instability of the electrolyte (Supporting Information Figure S14). The high cycling stability at low scan rate (1 A g^{-1}) and the similarity of Nyquist plots before and after cycling (Supporting Information Figure S12d, e) again indicate the electrolyte stability.

We further provided a Ragone plot (Figure 5a,b) of supercapacitors fabricated using the optimized ac-Gr/SWCNT films. The samples exhibited the highest volumetric energy density of 117.2 Wh L^{-1} (based on total thickness of active material in two electrodes) at a maximum power density of 424 kW L^{-1} (red star in Figure 5a) (see also Supporting Information Table S3), outperforming existing data in the literature. Our measured energy and power density (red squares) are reasonable with a small degradation of volumetric energy density while reaching a volumetric power density of 50.2 kW L^{-1}. The relatively small sacrifice in the energy density while maintaining high power density is another evidence of fast ion relaxation, originating from our 3D architecture of the optimized ac-Gr/SWCNT film. It is remarkable to observe that our structure still maintains high gravimetric energy and power density (Figure 5b). Although the thickness of the optimized ac-Gr/SWCNT film is thin (~6 μm), this film is free-standing by itself and can be used directly as supercapacitor electrodes without using binders and collectors. The thickness could be controlled from 1 μm to a 100 μm by varying the SWCNT and GO solution concentration and volume, which can further improve the electrochemical energy storage of the final package.

As seen in the Cartesian plot (Figure 5c), the mass density of our electrode is located in the middle with a value of 1.06 g cm^{-3}, leading to both high volumetric and gravimetric energy density. The reasonable mass density is the key factor not to sacrifice either volumetric or gravimetric density. For example, oriented graphene hydrogel (ref 11) and laser-scribed graphene (ref 12) show high gravimetric energy and power density, but volumetric energy and power densities are relatively low due to their low mass densities (0.069 and 0.048 g cm^{-3}, respectively). On the other hand, both

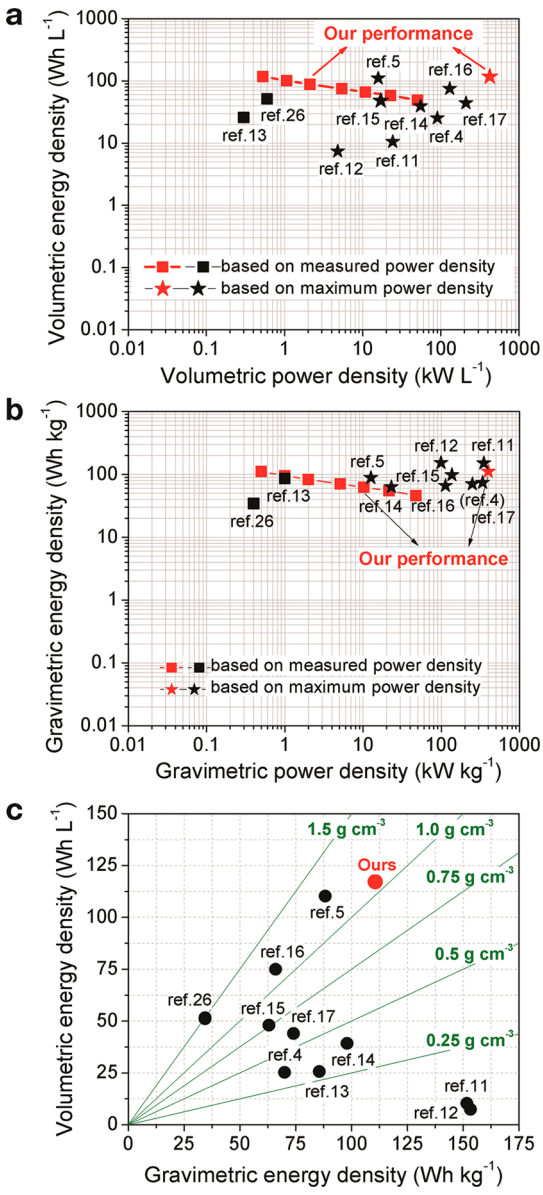

Figure 5. Energy and power densities of supercapacitors based on total thickness or weight of the optimized ac-Gr/SWCNT film compared to others reported. Ragone plot showing (a) volumetric energy density *versus* power density and (b) gravimetric energy density *versus* power density. (c) Cartesian diagram of the volumetric energy density *versus* the gravimetric energy density.

energy and power density (volumetric and gravimetric) of aligned-a-MEGO (ref 16) and as-MEGO (ref 17) are lower than our values but still maintain relatively high values due to their reasonable mass densites (1.15 and 0.59 g cm^{-3}, respectively). High volumetric and gravimetric energy density was obtained from EM-CCG (ref 5) due to its reasonable mass density (1.25 g cm^{-3}), but poor power density was retained due to its low intrinsic conductivity.

The remarkable electrochemical performance of the optimized ac-Gr/SWCNT sample was ascribed to the uniquely defined, CNT-bridged graphene 3D building block. SWCNTs easily intercalated into the GO *via* Coulombic interactions. Some nanotubes may overlap when the SWCNTs are long or their density is high (Supporting Information Figure S15). In such cases, the SWCNTs can bend because of the strong Coulombic repulsion between overlapping SWCNTs, which leads them to protrude from the surface. The next addition of SWCNTs then aligns parallel to the bent SWCNTs, which preferentially orients the liquid crystalline phase perpendicular to the graphene plane. This involves the competition process between electrostatic repulsion energy and mechanical bending energy. The underlying mechanism for the alignment of SWCNTs could be further complicated by several other factors, for instance, different lengths and diameters of CNTs and pH of the solution. This requires further study. Despite these well-defined 3D building blocks, a high charge storage capacity was not easily realized due to inefficient ion diffusion through the planar graphene layers in the nonactivated Gr/SWCNT film. KOH activation plays an important role in creating nanoscale pores in the graphene layers, which enhance the surface area and ion accessibility.

CONCLUSION

Our ac-SWCNT/Gr 3D building blocks created *via* robust electrostatic self-assembly and KOH activation shed light on how to design various synergistic nanostructure hybrids and provide a shortcut to realizing industrial ultrafast supercapacitors with high volumetric and gravimetric energy densities. The self-assembly approach of SWCNT/Gr hybrids in solution can lead to mass production with controllable CNT density or mass density without difficulty, which is advantageous over the CVD-grown CNT/graphene hybrids. Our approach is technologically more feasible than the CVD approach. Moreover, the high flexibility and exceptional electrical conductivity of these hybrid nanoporous films are promising for the development of flexible and wearable energy storage devices in the near future.

EXPERIMENTAL SECTION

Synthesis of the GO Solution. Graphite oxide was synthesized from graphite using a previously reported modification of Hummer's method.[40,41] The synthesized graphite oxide powder was sonicated in DI water for 1 h using a homogenizer (Sonosmasher ULH 700S, ULSSO Hi-Tech, Korea) with a power of 350 W and then centrifuged at 7191*g* (8000 rpm) for 10 min to remove any undispersed carbon flakes and impurities (VS-18000 M with V506A, VISION, Korea). This solution was freeze-dried at −50 °C (Freeze-Dryer, TFD series, ilShinBioBase, Korea) to obtain the purified graphite oxide powder. A graphene oxide solution (0.5 mg mL^{-1}) was then prepared by dispersing the purified graphite oxide powder in DI water for 45 min using the homogenizer with a power of 350 W. This GO solution has a natural pH of 4 and was used directly for experiments.

Synthesis of the CTAB-Grafted SWCNT Solution. Hipco SWCNTs (P grade, < 15% Fe) were purchased from Unidym.co, US. First, cetyltrimethylammonium bromide (>99%, SigmaAldrich)

was dissolved in DI water (0.1 wt %), and then, the SWCNT powder was added. The primary SWCNT solution concentration was 0.5 mg mL^{-1}. The CTAB and SWCNT mixture was sonicated for 2 h using a homogenizer with a power of 350 W. After removing the undispersed SWCNT bundles by centrifuging for 10 min at 7191*g* (8000 rpm), the CTAB-grafted SWCNT (denoted as CTAB-SWCNT) solution had a concentration of 0.3 mg mL^{-1} (measured by the absorption spectrum) and a natural pH of 7 and was used directly for experiments.

Synthesis of the ac-Gr/SWCNT Films. First, the GO solution was mixed with the CTAB-SWCNT solution. The mixture was then gently stirred at 250 rpm for 1 h, and a concentration-controlled KOH solution was added then stirred for 15 min. The mixture was vacuum-filtered through a polytetrafluoroethylene membrane (Millipore, 0.1 μm pore size). The film-type samples were then carefully peeled from the filter membrane and dried in a vacuum oven at 90 °C for 12 h. The resulting free-standing CTAB-SWCNT/GO/KOH films were placed in a horizontal tube furnace (50 mm diameter). The temperature was increased to 280 °C for 30 min, then to 800 °C at a ramping rate of 5 °C min^{-1}, and held there for 1 h under a nitrogen gas flow of 500 sccm. After cooling, the samples were washed by 10% acetic acid and DI water several times until a pH of 7 was reached. Finally, the ac-Gr/SWCNT films were obtained by drying in a vacuum oven at 120 °C for 12 h.

Synthesis of the Nonactivated Gr/SWCNT Films. The films were prepared also using a GO/SWCNT mass ratio of 3:1 and the same fabrication procedure as the ac-Gr/SWCNT films (see Supporting Information Figure S1) but without the KOH activation (step 3). The resulting films have a mass density of ~1.13 g cm^{-3}.

Synthesis of the SDS-SWCNT/Gr Film. Sodium dodecyl sulfate (SDS, >99%, SigmaAldrich) was used as a surfactant to disperse the SWCNTs into DI water instead of CTAB. The GO/SWCNT ratio was held at 3:1, the same as for the CTAB-SWCNT/Gr. The sample was annealed at 300 °C for 1 h under a N_2 atmosphere. Because the negatively charged SDS headgroup is similar to that of GO, all of the SDS-SWCNTs were randomly distributed on the graphene layers without intercalation. The resulting films have a mass density of ~1.48 g cm^{-3}.

Characterization Methods. The morphological and elemental analyses were performed *via* field emission scanning electron microscopy (FESEM, JEOL JSM7000F, Japan) and energy dispersive X-ray spectroscopy (Oxford-Horiba Inca XMax50). The nanostructure of the samples was investigated by HR-TEM (JEM 2100F, JEOL). The X-ray diffraction patterns were collected using a Rigaku SmartLab X-ray diffractometer (Cu Kα radiation, λ = 0.154 06 nm). Raman spectroscopy was performed using a micro-Raman system (Renishaw, RM1000-In Via, UK) with a laser wavelength of 532 nm. Polarized Raman spectroscopy (NTEGRA Spectra, NT-MDT, The Netherlands) was used to confirm the SWCNT alignment using laser light (532 nm) on the sample cross-section. The polarized angle was tested from 0° to 90° for wave numbers ranging from 1000 to 1700 cm^{-1}. The specific surface area was measured *via* liquid nitrogen cryosorption (Micromeritics ASAP2020, USA) using the BET method. The micropore and mesopore size distributions were estimated *via* the Horvath−Kawazoe (HK) and Barrett−Joyner-Halenda (BJH) methods, respectively. The lateral size and height profile of the GO sheets were characterized *via* atomic force microscopy (AFM, SPA-400, Seiko, Japan). Absorption and fluorescence spectra of the SWCNT solution were obtained using a nanospectralyzer system (NS2, Applied NanoFluorescence, Korea). The SWCNT concentration was calculated using the absorbance relationship $A = \varepsilon\rho L$ or $\rho = (A/A_o)\rho_o$, where A_o and A are the initial and final absorbances, respectively, ρ_o and ρ are the initial and final SWCNT concentrations, respectively, ε is the extinction coefficient, and L is the light path length.[42] To measure the initial absorbance, A_o, a well-dispersed solution with a low SWCNT concentration of 0.01 mg mL^{-1} (taken as ρ_o) was prepared. The sheet resistances (R_s) of the ac-Gr/SWCNT films were measured *via* a four-point probe Van der Pauw method using a multimeter (Keithley, model 2700, Korea). The conductivities (σ) of the films were calculated using the formula $\sigma = 1/(4.532 \times t \times R_s)$, where t represents the film thickness.[43] The zeta potentials and SWCNT length distributions were measured by electrophoretic light scattering (ELS-8000, Otsuka Electronics, Japan).

Characterization of Supercapacitors. Prototype supercapacitors were constructed using CR2032 coin cells reported previously.[32] The samples were punched into round electrodes of 0.8 cm in diameter. The loading mass was controlled from 0.6 to 1 mg cm^{-2}. Two symmetric electrodes were isolated using an ion-porous separator (Grade GF/C, Whatman, Korea). The neat ionic liquid 1-ethyl-3-methylimidazolium tetrafluoroborate (EMIM BF_4, SigmaAldrich), which has an electrochemical window from −2.2 to 3.5 V, was used as the electrolyte. The supercapacitor measurements were performed using a VMP3 electrochemical workstation (Bio-Logic Science Instruments, France).

The imaginary part of the complex capacitance was calculated from the impedance data using the following formula:

$$C'' = \frac{Z'}{\omega|Z|^2} \tag{1}$$

Here, $C = C' - jC''$ and $Z = Z' + jZ''$, where C and Z are the total effective capacitance and impedance for the supercapacitors, respectively; C' and Z' are the respective real parts and C'' and Z'' are the respective imaginary parts of the total effective capacitance and impedance for the supercapacitors; ω is the angular frequency; and j is an imaginary number.[38]

The gravimetric specific capacitance (C_s) was calculated from the CV measurements using the following formula:

$$C_s = \frac{2}{m_e} \times \frac{|Q_c| + |Q_d|}{2V} \tag{2}$$

where $|Q_c|$ and $|Q_d|$ are the charges stored in the anode and cathode cycles, respectively, m_e is the active mass for each electrode, and V is the potential window.[44]

C_s was also calculated from CD measurements as follows:

$$C_s = \frac{2I}{m_e \frac{dV}{dt}} = \frac{2I_s}{\frac{dV}{dt}} \tag{3}$$

where I is the constant current applied, dV/dt is the slope obtained by fitting a straight line to the discharge curve, m_e is the active mass for each electrode, and I_s is the current density.[5]

The gravimetric energy density (E) and gravimetric average power density (P_{av}) were calculated from the CD measurements using the following formulas:

$$E = \frac{C_s \times V^2}{8} \text{ and } P_{av} = \frac{E}{\Delta t} \tag{4}$$

where V is the operating voltage and Δt is the discharge time.

The maximum gravimetric power density (P_{max}) was estimated from the CD measurements using the following equation:

$$P_{max} = \frac{(V - V_{drop})^2}{4m \times ESR} \tag{5}$$

where V is the operating voltage, V_{drop} is the voltage drop at the beginning of the discharge, m is the total active mass of the two electrodes, and ESR is the equivalent series resistance calculated using the formula $ESR = V_{drop}/(2I)$, where I is the constant current applied.[4]

The volumetric values for the specific capacitance, energy density, average power density, and maximum power density were calculated as follows:

$$X = \rho Y \tag{6}$$

where ρ is the sample density, X is the volumetric value, and Y is the gravimetric value.

Conflict of Interest: The authors declare no competing financial interest.

Supporting Information Available: Supporting Information detailing experimental methods, supplementary text, Figures S1−S15, Tables 1−3, and references. This material is available free of charge *via* the Internet at http://pubs.acs.org.

Acknowledgment. This work was supported by the Institute for Basic Science (EM1304) and in part by the HRD Program (No. 20124010203270) of the KETEP grant funded by the Korean Ministry of Knowledge Economy.

REFERENCES AND NOTES

1. Conway, B. E. *Electrochemical Supercapacitors: Scientific Fundamentals and Technological Applications*; Kluwer Academic/Plenum: New York, 1999.
2. Miller, J. R.; Simon, P. Electrochemical Capacitors for Energy Management. *Science* **2008**, *321*, 651–652.
3. Burke, A. R&D Considerations for the Performance and Application of Electrochemical Capacitors. *Electrochim. Acta* **2007**, *53*, 1083–1091.
4. Zhu, Y.; Murali, S.; Stoller, M. D.; Ganesh, K. J.; Cai, W.; Ferreira, P. J.; Pirkle, A.; Wallace, R. M.; Cychosz, K. A.; Thommes, M.; *et al*. Carbon-Based Supercapacitors Produced by Activation of Graphene. *Science* **2011**, *332*, 1537–1541.
5. Yang, X.; Cheng, C.; Wang, Y.; Qiu, L.; Li, D. Liquid-Mediated Dense Integration of Graphene Materials for Compact Capacitive Energy Storage. *Science* **2013**, *341*, 534–537.
6. Noorden, R. V. The Rechargeable Revolution: A Better Battery. *Nature* **2014**, *507*, 26–28.
7. Simon, P.; Gogotsi, Y. Materials for Electrochemical Capacitors. *Nat. Mater.* **2008**, *7*, 845–854.
8. Segal, M. Selling Graphene by the Ton. *Nat. Nanotechnol.* **2009**, *4*, 612–614.
9. Sun, Y.; Wu, Q.; Shi, G. Graphene Based New Energy Materials. *Energy Environ. Sci.* **2011**, *4*, 1113–1132.
10. Liu, C.; Yu, Z.; Neff, D.; Zhamu, A.; Jang, B. Z. Graphene-Based Supercapacitor with an Ultrahigh Energy Density. *Nano Lett.* **2010**, *10*, 4863–4868.
11. Yang, X.; Zhu, J.; Qiu, L.; Li, D. Bioinspired Effective Prevention of Restacking in Multilayered Graphene Films: Towards the Next Generation of High-Performance Supercapacitors. *Adv. Mater.* **2011**, *23*, 2833–2838.
12. El-Kady, M. F.; Strong, V.; Dubin, S.; Kaner, R. B. Laser Scribing of High-Performance and Flexible Graphene-Based Electrochemical Capacitors. *Science* **2012**, *335*, 1326–1330.
13. Zhang, L. L.; Zhao, X.; Stoller, M. D.; Zhu, Y.; Ji, H.; Murali, S.; Wu, Y.; Perales, S.; Clevenger, B.; Ruoff, R. S. Highly Conductive and Porous Activated Reduced Graphene Oxide Films for High-Power Supercapacitors. *Nano Lett.* **2012**, *12*, 1806–1812.
14. Zhang, L.; Zhang, F.; Yang, X.; Long, G.; Wu, Y.; Zhang, T.; Leng, K.; Huang, Y.; Ma, Y.; Yu, A.; *et al*. Porous 3D Graphene-Based Bulk Materials with Exceptional High Surface Area and Excellent Conductivity for Supercapacitors. *Sci. Rep.* **2013**, *3*, 1408.
15. Murali, S.; Quarles, N.; Zhang, L. L.; Potts, J. R.; Tan, Z.; Lu, Y.; Zhu, Y.; Ruoff, R. S. Volumetric Capacitance of Compressed Activated Microwave-Expanded Graphite Oxide (a-MEGO) Electrodes. *Nano Energy* **2013**, *2*, 764–768.
16. Ghaffari, M.; Zhou, Y.; Xu, H.; Lin, M.; Kim, T. Y.; Ruoff, R. S.; Zhang, Q. M. High-Volumetric Performance Aligned Nano-Porous Microwave Exfoliated Graphite Oxide-Based Electrochemical Capacitors. *Adv. Mater.* **2013**, *25*, 4879–4885.
17. Kim, T.; Jung, G.; Yoo, S.; Suh, K. S.; Ruoff, R. S. Activated Graphene-Based Carbons as Supercapacitor Electrodes with Macro- and Mesopores. *ACS Nano* **2013**, *7*, 6899–6905.
18. Lukatskaya, M. R.; Mashtalir, O.; Ren, C. E.; Dall'Agnese, Y.; Rozier, P.; Taberna, P. L.; Naguib, M.; Simon, P.; Barsoum, M. W.; Gogotsi, Y. Cation Intercalation and High Volumetric Capacitance of Two-Dimensional Titanium Carbide. *Science* **2013**, *341*, 1502–1505.
19. Ghidiu, M.; Lukatskaya, M. R.; Zhao, M.-Q.; Gogotsi, Y.; Barsoum, M. W. Conductive Two-Dimensional Titanium Carbide 'Clay' with High Volumetric Capacitance. *Nature* **2014**, *516*, 78–81.
20. Pumera, M. Graphene-Based Nanomaterials for Energy Storage. *Energy Environ. Sci.* **2011**, *4*, 668–674.
21. Fan, Z.; Yan, J.; Zhi, L.; Zhang, Q.; Wei, T.; Feng, J.; Zhang, M.; Qian, W.; Wei, F. A Three-Dimensional Carbon Nanotube/Graphene Sandwich and Its Application as Electrode in Supercapacitors. *Adv. Mater.* **2010**, *22*, 3723–3728.
22. Yu, D.; Dai, L. Self-Assembled Graphene/Carbon Nanotube Hybrid Films for Supercapacitors. *J. Phys. Chem. Lett.* **2009**, *1*, 467–470.
23. Jha, N.; Ramesh, P.; Bekyarova, E.; Itkis, M. E.; Haddon, R. C. High Energy Density Supercapacitor Based on a Hybrid Carbon Nanotube-Reduced Graphite Oxide Architecture. *Adv. Energy Mater.* **2012**, *2*, 438–444.
24. Cheng, Q.; Tang, J.; Ma, J.; Zhang, H.; Shinya, N.; Qin, L.-C. Graphene and Carbon Nanotube Composite Electrodes for Supercapacitors with Ultra-High Energy Density. *Phys. Chem. Chem. Phys.* **2011**, *13*, 17615–17624.
25. Wang, Y.; Wu, Y.; Huang, Y.; Zhang, F.; Yang, X.; Ma, Y.; Chen, Y. Preventing Graphene Sheets from Restacking for High-Capacitance Performance. *J. Phys. Chem. C* **2011**, *115*, 23192–23197.
26. Jung, N.; Kwon, S.; Lee, D.; Yoon, D.-M.; Park, Y. M.; Benayad, A.; Choi, J.-Y.; Park, J. S. Synthesis of Chemically Bonded Graphene/Carbon Nanotube Composites and Their Application in Large Volumetric Capacitance Supercapacitors. *Adv. Mater.* **2013**, *25*, 6854–6858.
27. Byon, H. R.; Lee, S. W.; Chen, S.; Hammond, P. T.; Shao-Horn, Y. Thin Films of Carbon Nanotubes and Chemically Reduced Graphenes for Electrochemical Micro-Capacitors. *Carbon* **2011**, *49*, 457–467.
28. Beidaghi, M.; Wang, C. Micro-Supercapacitors Based on Interdigital Electrodes of Reduced Graphene Oxide and Carbon Nanotube Composites with Ultrahigh Power Handling Performance. *Adv. Funct. Mater.* **2012**, *22*, 4501–4510.
29. Wu, Y.; Zhang, T.; Zhang, F.; Wang, Y.; Ma, Y.; Huang, Y.; Liu, Y.; Chen, Y. In Situ Synthesis of Graphene/Single-Walled Carbon Nanotube Hybrid Material by Arc-Discharge and Its Application in Supercapacitors. *Nano Energy* **2012**, *1*, 820–827.
30. Lin, J.; Zhang, C.; Yan, Z.; Zhu, Y.; Peng, Z.; Hauge, R. H.; Natelson, D.; Tour, J. M. 3-Dimensional Graphene Carbon Nanotube Carpet-Based Microsupercapacitors with High Electrochemical Performance. *Nano Lett.* **2012**, *13*, 72–78.
31. Zhu, Y.; Li, L.; Zhang, C.; Casillas, G.; Sun, Z.; Yan, Z.; Ruan, G.; Peng, Z.; Raji, A.-R. O.; Kittrell, C.; *et al*. A Seamless Three-Dimensional Carbon Nanotube Graphene Hybrid Material. *Nat. Commun.* **2012**, *3*, 1225.
32. Yao, F.; Güneş, F.; Ta, H. Q.; Lee, S. M.; Chae, S. J.; Sheem, K. Y.; Cojocaru, C. S.; Xie, S. S.; Lee, Y. H. Diffusion Mechanism of Lithium Ion through Basal Plane of Layered Graphene. *J. Am. Chem. Soc.* **2012**, *134*, 8646–8654.
33. White, B.; Banerjee, S.; O'Brien, S.; Turro, N. J.; Herman, I. P. Zeta-Potential Measurements of Surfactant-Wrapped Individual Single-Walled Carbon Nanotubes. *J. Phys. Chem. C* **2007**, *111*, 13684–13690.
34. Li, D.; Muller, M. B.; Gilje, S.; Kaner, R. B.; Wallace, G. G. Processable Aqueous Dispersions of Graphene Nanosheets. *Nat. Nanotechnol.* **2008**, *3*, 101–105.
35. Pandey, D.; Reifenberger, R.; Piner, R. Scanning Probe Microscopy Study of Exfoliated Oxidized Graphene Sheets. *Surf. Sci.* **2008**, *602*, 1607–1613.
36. Lei, Z.; Christov, N.; Zhao, X. S. Intercalation of Mesoporous Carbon Spheres between Reduced Graphene Oxide Sheets for Preparing High-Rate Supercapacitor Electrodes. *Energy Environ. Sci.* **2011**, *4*, 1866–1873.
37. Zhao, M.-Q.; Liu, X.-F.; Zhang, Q.; Tian, G.-L.; Huang, J.-Q.; Zhu, W.; Wei, F. Graphene/Single-Walled Carbon Nanotube Hybrids: One-Step Catalytic Growth and Applications for High-Rate Li−S Batteries. *ACS Nano* **2012**, *6*, 10759–10769.
38. Ghosh, A.; Le, V. T.; Bae, J. J.; Lee, Y. H. TLM-PSD Model for Optimization of Energy and Power Density of Vertically Aligned Carbon Nanotube Supercapacitor. *Sci. Rep.* **2013**, *3*, 2939.
39. Xia, J.; Chen, F.; Li, J.; Tao, N. Measurement of the Quantum Capacitance of Graphene. *Nat. Nanotechnol.* **2009**, *4*, 505–509.

40. Hummers, W. S.; Offeman, R. E. Preparation of Graphitic Oxide. *J. Am. Chem. Soc.* **1958**, *80*, 1339–1339.
41. Cote, L. J.; Kim, F.; Huang, J. Langmuir-Blodgett Assembly of Graphite Oxide Single Layers. *J. Am. Chem. Soc.* **2008**, *131*, 1043–1049.
42. Biswas, C.; Kim, K. K.; Geng, H.-Z.; Park, H. K.; Lim, S. C.; Chae, S. J.; Kim, S. M.; Lee, Y. H.; Nayhouse, M.; Yun, M. Strategy for High Concentration Nanodispersion of Single-Walled Carbon Nanotubes with Diameter Selectivity. *J. Phys. Chem. C* **2009**, *113*, 10044–10051.
43. Wu, Z. S.; Parvez, K.; Feng, X.; Müllen, K., Graphene-Based In-Plane Micro-Supercapacitors with High Power and Energy Densities. *Nat. Commun.* **2013**, 4.
44. Ghosh, A.; Ra, E. J.; Jin, M.; Jeong, H.-K.; Kim, T. H.; Biswas, C.; Lee, Y. H. High Pseudocapacitance from Ultrathin V_2O_5 Films Electrodeposited on Self-Standing Carbon-Nanofiber Paper. *Adv. Funct. Mater.* **2011**, *21*, 2541–2547.